


 Cite this: *RSC Adv.*, 2025, 15, 48994

Enhanced degradation of doxycycline by citric acid-functionalized graphitic carbon nitride decorated with MIL-88A and FeS: optimization, degradation mechanism, and degradation pathway

 Abdelazeem S. Eltaweil,^{ab} Mohammed Salah Ayoup,^c Jawaher Y. Al Nawah^{bc} and Eman M. Abd El-Monaem^{bd}

This investigation provides a new Fenton-like heterogeneous catalyst construct, citric acid-functionalized graphitic carbon nitride decorated with MIL-88A and iron sulfide (FeS/MIL-88A@Cit-gCN). The characteristics of FeS_{0.5}/MIL-88A_{0.5}@Cit-gCN were scrutinized using different instruments to identify its surface charge, morphology, elemental and structural compositions, and crystallinity. The catalytic activity of FeS_{0.5}/MIL-88A_{0.5}@Cit-gCN was inspected by a series of adsorption/Fenton-like experiments, evaluating the best catalytic parameters for efficiently decomposing doxycycline (Dox). The maximum adsorption% and decomposition% of Dox were 48.78% and 99.40%, respectively, at H₂O₂ concentration = 100 mg L⁻¹, system temperature = 20 °C, pH = 5, and FeS_{0.5}/MIL-88A_{0.5}@Cit-gCN dose = 0.01 g. The second-order kinetic model best represented the Dox decomposition process by FeS_{0.5}/MIL-88A_{0.5}@Cit-gCN. The decomposition mechanism of Dox proceeded by a catalytic radical pathway, and most probably, ·OH was the governing radical in the catalytic medium. The ·OH radicals were produced through the contribution of the iron, sulfur, and electron-donor groups of FeS_{0.5}/MIL-88A_{0.5}@Cit-gCN to activate H₂O₂. The adsorption reaction played an excellent role in the decomposition capacity of Dox since the drug molecules were attached to the FeS_{0.5}/MIL-88A_{0.5}@Cit-gCN surface by n-π interactions, coulombic interactions, and coordination bonds. The recycling study denoted the durability of FeS_{0.5}/MIL-88A_{0.5}@Cit-gCN after reusing for five times. These results render FeS_{0.5}/MIL-88A_{0.5}@Cit-gCN a premium heterogeneous catalyst that can be applied at an industrial scale.

 Received 19th September 2025
 Accepted 14th November 2025

DOI: 10.1039/d5ra07120h

rsc.li/rsc-advances

1. Introduction

Drinking water shortage is an apprehending global concern due to the prevalence of pollution in most water resources. One of the biggest sources of water pollution is antibiotic residues, such as doxycycline (Dox), which is an exceptional anti-inflammatory and anti-apoptotic drug suitable for treating the current pandemic diseases.^{1,2} Large Dox quantities are used daily for curing infections, such as those in the stomach, skin, urinary tract, and respiratory tract. Meanwhile, about half of the Dox dosages cannot be digested by the human body and are excreted *via* urine.³ For this sake, environmental researchers are engaged in ameliorating the efficacy of wastewater remediation processes. Amongst them, the Fenton process is an advanced

hydroxyl radical (·OH)-based oxidation reaction that involves decomposing toxic organic contaminants into eco-friendly compounds.^{4,5} The Fenton reaction proceeds through the activation of hydrogen peroxide (H₂O₂) by iron catalysts to produce ·OH, which is responsible for attacking the targeted organic pollutants in the catalytic medium.⁶ Nevertheless, the catalytic activity of iron catalysts and their redox Fe²⁺/Fe³⁺ cycle still needs further improvement.⁷ Notably, several studies have recommended the remarkable catalytic efficiency of non-iron (Fenton-like) catalysts, including layered double hydroxides, metal oxides/sulfides, carbon materials, and metal-organic frameworks.⁸

Graphitic carbon nitride (gCN) is a layer-shaped polymer that is prepared *via* pyrolyzing nitrogen-containing substances, such as dicyandiamide, cyanamide, melamine, guanidine hydrochloride, and urea.⁹ Pioneering studies have suggested that urea-derived gCN could be a better choice than other nitrogen-containing substances, as urea is an eco-friendly and low-cost substance, which makes it appropriate for large-scale applications.¹⁰ In addition, the self-supported gas preparation approach using urea as a precursor is distinguished from other

^aDepartment of Engineering, Faculty of Technology and Engineering, University of Technology and Applied Sciences, Ibra, Sultanate of Oman

^bChemistry Department, Faculty of Science, Alexandria University, Alexandria, Egypt

^cDepartment of Chemistry, College of Science, King Faisal University, Al-Ahsa 31982, Saudi Arabia. E-mail: jalnawah@kfu.edu.sa

^dAdvanced Technology Innovation, Borg El-Arab, Alexandria, Egypt. E-mail: emanabdelmonaem5925@yahoo.com



template synthetic methods, in which urea produces gas bubbles during thermal treatment that act as a soft template and facilitate the formation of porous microstructures.¹¹ Furthermore, this produced gas has another significant role in the processing carbon nitride condensation.¹² Notably, by comparing the soft-template approach to the other template approaches, it was deduced that the soft-template approach has simple processing, does not form impurities, and is suitable to yield a porous microstructure.

The structure of gCN is composed of arranged tri-s-triazine units, each comprising six nitrogen atoms.¹³ The gCN possesses several interesting merits, including high chemical stability, low costs, eco-benign properties, a high surface area, facile accessibility, and excellent catalytic activity.¹⁴ The individual structure of gCN contains many lone pairs of electrons, making it an outstanding Fenton-like catalyst. Moreover, the structural flexibility of gCN eases fostering its catalytic Fenton-like activity by forming a composite or functionality. Citric acid (Cit) serves as a potent chelating agent and exhibits remarkable Fenton-like catalytic activity, making it suitable for the functionalization of gCN. Citric acid is a short-chain carboxylic acid that contains abundant carboxyl and hydroxyl groups.^{15,16} Surprisingly, citric acid has demonstrated excellent performance in the Fenton-like degradation of organic pollutants, as it can activate H₂O₂ by sharing its ample electrons. Additionally, citric acid is a chelating agent; so, it can easily chelate contaminants on its surface.¹⁷ Notably, citric acid possesses a significant chelation property towards iron species, which prevents iron precipitation at higher pH values.¹⁸

Several published papers have documented the good Fenton-like catalytic activity of gCN for degrading pharmaceutical drugs. In this context, Haroon *et al.*¹⁹ fabricated Fe₃O₄-doped gCN to degrade TC *via* a Fenton-like reaction. The maximum decomposition% of TC by Fe₃O₄-doped gCN was 90.00% when the doped Fe₃O₄ percentage was 20%. The magnetic character enhanced the recyclability of Fe₃O₄-doped gCN, and the recycling test elucidated a slight decline in its activity after reuse in the decomposition reaction of TC. Furthermore, Mu *et al.*²⁰ studied the catalytic activity of magnetic Fe-gCN for Fenton-like degradation of APAP, implying that the decomposition% was nearly 100% after 30 minutes over a wide pH scale. In another study, Liu and his co-authors²¹ focused on photo-Fenton degradation of Dox by gCN@MIL-100 in the persulfate and H₂O₂ systems. The degradation percentages of Dox by activating persulfate and H₂O₂ using gCN@MIL-100 were 82.80% and 69.20% after 30 minutes, respectively. This result was attributed to the generation of higher active radicals by persulfate than by H₂O₂.

In the recent decade, bountiful MOF families have been deemed superb candidates for applications in various sectors, including gas separation, solar cells, drug delivery, catalysis, sensors, and others.^{22,23} MOFs possess discernible properties, including a high surface area, excellent mechanical and thermal behavior, a porous structure, and easy functionalization. Noteworthy, the chemical structures of MOFs render them remarkable Fenton/Fenton-like catalysts because they comprise unsaturated metal ions and active oxygen groups.²⁴ Because of the auspicious catalytic activity, excellent chemical structure,

and reusability of MIL-88A, it exhibited promising results when it was applied in the Fenton degradation reactions of many toxic organic pollutants.²⁵ Based on the synthesis approach of MIL-88A, it is classified as a hexagonal MIL-88A when prepared by the solvothermal method using *N,N*-dimethylformamide as the reaction solvent. Similarly, the rod-shaped MIL-88A is fabricated *via* the hydrothermal method in an aqueous medium, which is a favorable preparation process owing to the usage of an eco-friendly solvent.^{26,27}

Diverse investigations have reported the high catalytic activity of MIL-88A toward pharmaceutical drugs; for instance, Shi *et al.*²⁸ decorated MIL-88A with MgFe₂O₄ to design a magnetic catalyst by a ball-milling method. The MgFe₂O₄/MIL-88A catalyst showed remarkable photo-Fenton catalytic activity for degrading SMX, in which the decomposition percentage reached 99.80% after 20 minutes. Furthermore, Wang and his co-workers²⁹ engineered the photo-Fenton MIL-88A/cotton fiber catalyst for decomposing tetracyclines. The degradation percentages of OTC, TC, and CTC by activating PDS using MIL-88A/cotton fibers in the presence of UV light were 97.5%, 95.2%, and 100.0%, respectively. In this context, Eltaweil *et al.*³⁰ synthesized Ce-decorated MIL-88A/gCN to decompose TC *via* the oxidative Fenton-like reaction. The experimental results demonstrated a synergistic effect between adsorption and Fenton-like decomposition reactions, where the adsorption% and decomposition% of TC were 51.96% and 92.44%, respectively, in a neutral pH medium. Although MIL-88A has been applied in the photo-Fenton/Fenton degradation of many pharmaceutical drugs, it has not yet been applied in the Fenton decomposition of Dox.

Metal sulfides are materials built *via* a coordination bond between an earth-rich metal (*viz.*, strontium, iron, copper, tin, and nickel) and sulfur species.³¹ Metal sulfides can be prepared *via* many approaches, such as thermal decomposition, precipitation, ball milling, and hydrothermal and electrochemical approaches.³² Metal sulfides have shown remarkable outcomes in various fields, including catalysis, CO₂ reduction, supercapacitors, oxygen generation reactions, and lithium-ion batteries.^{4,5} Furthermore, the prime catalytic activity of metal sulfides in Fenton/Fenton-like processes is due to their being electron-rich nature with good chemical stability and electric conductivity.³³ The sulfur species of metal sulfides boost the electron transfer from unsaturated metal ions to H₂O₂ molecules, which increases the concentration of the yielded ·OH.^{34,35}

Despite the outstanding catalytic performance of metal sulfides, there is a lack of published research that investigates the Fenton/Fenton-like degradation of toxic pharmaceutical drugs by metal sulfides. In one attempt, Yang *et al.*³⁶ highlighted the decomposition of OTC by H₂O₂ activation using the RS-FeS and RSBC-FeS catalysts. The decomposition% of OTC by RS-FeS and RSBC-FeS were 70.14% and 79.35%, while their adsorption capacities were 635.66 and 827.80 mg g⁻¹, respectively. The mechanistic study demonstrated the contribution of both radical and non-radical degradation pathways in decomposing OTC by RS-FeS and RSBC-FeS. In another investigation, Cai *et al.*³⁷ studied the Fenton decomposition activity of FeS towards the TC drug, and the decomposition% achieved was 98.00%



within 30 minutes at pH = 3. The selectivity test revealed the higher selectivity for TC than that for TOC, with a decomposition% of 20.00% after 60 minutes.

Based on the literature review on the Fenton-like degradation activities of gCN, MIL-88A, and FeS, there is a scarcity of research papers that involve decomposing Dox. The conducted studies on decomposing Dox by gCN, MIL-88A, and FeS have applied the photo-Fenton reaction, but the Fenton degradation mechanism and degradation pathway in the dark have not been investigated. Accordingly, our research focused on boosting the Fenton-like catalytic activity of gCN by the Cit functionality, followed by binding Cit-gCN with iron-based catalysts like MIL-88A and FeS to yield the heterogeneous FeS/MIL-88A@Cit-gCN catalyst. Various characterization instruments were used for investigating the well-fabrication of FeS/MIL-88A@Cit-gCN and its chemical/physical properties. The optimization of the Fenton-like catalytic degradation of Dox by the FeS/MIL-88A@Cit-gCN catalyst was conducted through a series of adsorption/Fenton-like experiments under varied reaction conditions. The resultant experimental data were analyzed by first-order and second-order kinetics. The catalytic mechanism of Dox degradation by FeS/MIL-88A@Cit-gCN was determined using the scavenger test and the XPS spectra of the used and pristine catalysts. The recyclability of the FeS/MIL-88A@Cit-gCN catalyst was determined by performing the cycling test for six adsorption/Fenton-like runs for the Dox molecules.

2. Experimental work

2.1. Fabrication of Cit-gCN

First, gCN was prepared by the pyrolysis approach as follows: 5.0 g of urea was added to a sealed porcelain crucible and calcined at 550 °C for four hours in a muffle furnace at a heating rate of about 2 °C per minute. The crucible was cooled naturally, and then, the formed gCN was stored for later use. Second, 1 g of gCN was dispersed in 25 mL of distilled water under sonication for 15 minutes. 0.3 M Cit was added to the gCN suspension, followed by sonication for another 15 minutes. Then, the Cit-gCN suspension was kept overnight under slow stirring, allowing Cit and gCN to link together. The Cit-functionalized gCN was separated, rinsed to eliminate excess Cit, and dried at 60 °C in an air oven for 10 hours.

2.2. Fabrication of MIL-88A

1.4 g of FeCl₃·6H₂O and 0.58 g of fumaric acid were added to 60 mL of distilled water under high-rate stirring. After an hour, the light-orange solution of Fe³⁺/fumaric acid was added to the autoclave, followed by heating it at 85 °C for 24 hours. After cooling the autoclave in the air, the MIL-88A powder was collected using a centrifuge and washed with distilled water and ethanol. Ultimately, the wet MIL-88A powder was kept in an oven at 85 °C for drying.

2.3. The fabrication of FeS

2.00 g of FeCl₃·6H₂O and 1.15 g of SC(NH₂)₂ were added to 80 mL of a mixed solvent of H₂O and EG with a volume ratio of

3 : 1. The reaction solution was transferred into the autoclave and placed in an oven for heating at 190 °C for 6 hours. The formed black powder was centrifuged, rinsed with distilled water, and heated for 10 hours at 60 °C in an oven.³⁸

2.4. The fabrication of FeS/MIL-88A@Cit-gCN

In a container, Cit-gCN was suspended in 30 mL of distilled water using an ultrasonic water bath for 30 minutes. Next, FeS and MIL-88A were added to the Cit-gCN suspension, followed by sonication for another 15 minutes. The FeS/MIL-88A@Cit-gCN composite was centrifuged and dried at 70 °C for 10 hours. Three composites were fabricated with different mass ratios of FeS, MIL-88A, and Cit-gCN, named FeS_{0.5}/MIL-88A_{0.5}@Cit-gCN (0.5 : 0.5 : 1), FeS_{0.5}/MIL-88A@Cit-gCN_{0.5} (0.5 : 1:0.5), and FeS/MIL-88A_{0.5}@Cit-gCN_{0.5} (1 : 0.5 : 0.5).

2.5. Fenton-like degradation experiments of Dox

The catalytic parameters of the Fenton-like decomposition process of Dox by the heterogeneous FeS/MIL-88A@Cit-gCN catalyst were optimized as follows: (1) the decomposition efficiencies of Dox by FeS, MIL-88A, Cit-gCN, and FeS/MIL-88A@Cit-gCN composites were investigated to evidence the significance of the binding of the pure components in a composite form and to choose the best mass ratio of these components. (2) The appropriate pH medium for decomposing the Dox molecules efficiently was recorded after comparing the decomposition% of Dox at varied pH values of 3, 5, 7, 9, and 11. (3) The suitable concentration of H₂O₂ to decompose the Dox molecules was selected based on the experimental results of decomposing Dox by FeS/MIL-88A@Cit-gCN in the presence of H₂O₂ at concentrations of 10, 50, 100, and 200 mg L⁻¹ (4) The economical FeS/MIL-88A@Cit-gCN dose to decompose Dox with higher efficiency was determined by studying the process at different dosages of 5, 7.5, 10, and 15 mg. (5) The impact of the system temperature of Dox-FeS/MIL-88A@Cit-gCN was deduced at the temperatures of 20, 30, 40, and 50 °C. (6) The decomposition efficiency of FeS/MIL-88A@Cit-gCN for various Dox concentrations was identified in a concentration range from 50 to 300 mg L⁻¹. (7) The recycling test of the FeS/MIL-88A@Cit-gCN catalyst was conducted for six runs of the Dox adsorption/Fenton-like process by separating the catalyst after each run, washing it with an aqueous NaOH solution, and finally drying the composite before using it in the subsequent run. (8) The scavenging test of decomposing Dox by FeS/MIL-88A@Cit-gCN was executed in the presence of TCM and *t*-BuOH as quenchers for O₂^{·-} and ·OH, respectively.

After each experiment, the Dox solution was withdrawn to measure its concentration using a spectrophotometer (labeled as C_t) and taking into consideration the concentration of Dox before the degradation reaction (labeled as C₀) to calculate the decomposition% of Dox by eqn (1).

$$\text{Decomposition\%} = \frac{C_0 - C_t}{C_0} \times 100 \quad (1)$$



3. Results and discussion

3.1. Characterization of FeS_{0.5}/MIL-88A_{0.5}@Cit-gCN

3.1.1. FTIR. The compositions of FeS, MIL-88A, gCN, Cit-gCN, and FeS_{0.5}/MIL-88A_{0.5}@Cit-gCN were investigated by the FTIR instrument, as signaled in Fig. 1a. The gCN spectrum elucidated the peaks belonging to primary and secondary amines at 3212 and 3062 cm⁻¹, respectively. The absorption peaks of C=N and C-N were observed at 1722 and 1177 cm⁻¹, respectively, while the peak related to the gCN heptazine ring appeared at 782 cm⁻¹. In the Cit-gCN spectrum, the peaks corresponding to C-O and C=O were revealed at 1253 and 1580 cm⁻¹, respectively, indicating the Cit functionality on the gCN surface. In the MIL-88A spectrum, the peak corresponding to the Fe-O bond was manifested at 552 cm⁻¹, confirming the linkage of the Fe³⁺ species of the oxygenated groups of fumaric acid. Furthermore, the peaks of C-H and C-C were observed at 1212 and 982 cm⁻¹, respectively, which are assigned to the *trans*-diene of the -fumaric acid. In addition, the carboxyl group peaks of the fumaric acid appeared at 1551 and 1398 cm⁻¹, which were ascribed to asymmetric and symmetric carboxyl

vibrations, respectively. The broad peak centered at around 3400 cm⁻¹ was attributed to the hydroxyl of the adsorbed H₂O molecules.²³⁻²⁵ In the FeS spectrum, the absorption peak at 1453 cm⁻¹ was related to the C-N bond of SC(NH₂)₂, and the peaks at 463, 3437, and 1022 cm⁻¹ were attributed to Fe-S, O-H, and Fe-OH, respectively. The peaks of the S-S bond emerged at 616 and 1636 cm⁻¹, while the S-O peak appeared at 1117 cm⁻¹.³⁹⁻⁴¹ In the FeS_{0.5}/MIL-88A_{0.5}@Cit-gCN spectrum, the peaks belonging to FeS, MIL-88A, and Cit-gCN were observed, confirming their successful linkage inside the catalyst's matrix.

3.1.2. XRD. The crystallographic nature of FeS, MIL-88A, gCN, Cit-gCN, and FeS_{0.5}/MIL-88A_{0.5}@Cit-gCN was determined using the XRD characterization tool (Fig. 1b). In the XRD pattern of pure gCN, two characteristic peaks were observed at 2θ values of 19.77° and 29.73°, associated with the planes of (100) and (002), respectively, according to the Joint Committee on Powder Diffraction Standards (JCPDS) no. 87-1526.⁴² The Cit-gCN pattern showed the same pattern as gCN, which may be due to the low Cit concentration in the analyzed sample.⁴³ In the MIL-88A pattern, the corresponding peaks of MIL-88A emerged at 2θ of 10.77°, 11.98°, 12.94°, 15.37°, and 21.42°, belonging to

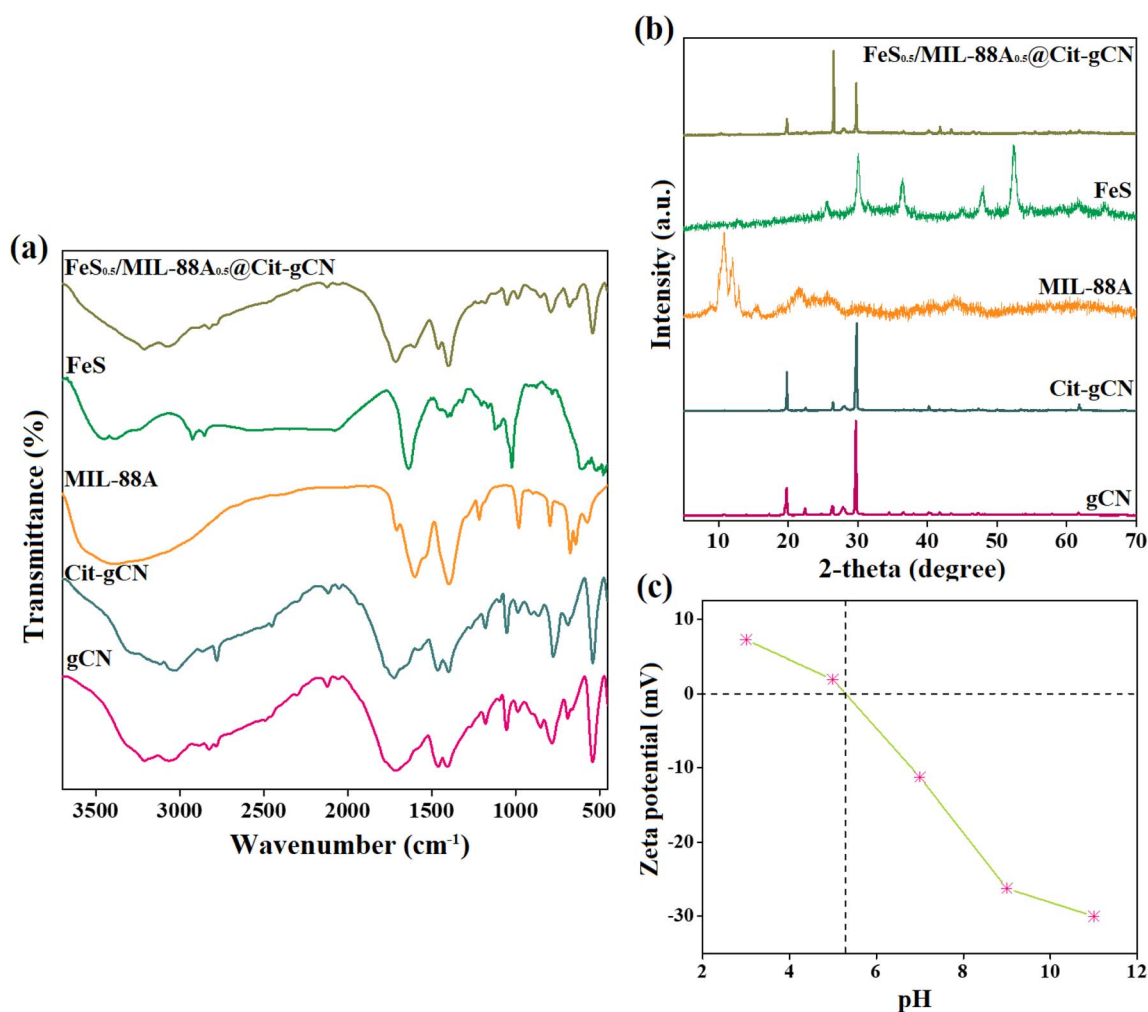


Fig. 1 (a) FTIR spectra of FeS, MIL-88A, gCN, Cit-gCN, and FeS_{0.5}/MIL-88A_{0.5}@Cit-gCN, (b) XRD patterns of FeS, MIL-88A, gCN, Cit-gCN, and FeS_{0.5}/MIL-88A_{0.5}@Cit-gCN, and (c) ZP of FeS_{0.5}/MIL-88A_{0.5}@Cit-gCN.



the (100), (101), (110), (012), and (022) planes, respectively.²⁹ In the FeS pattern, the diffraction peaks at 2θ of 25.57° , 30.06° , 36.40° , 47.88° , 52.41° , and 61.76° were related to the (111), (200), (211), (220), (311), and (023) planes from JCPDS no. 29-0723, respectively.⁴⁴ In the $\text{FeS}_{0.5}/\text{MIL-88A}_{0.5}/\text{Cit-gCN}$ pattern, a notable decline in the corresponding peaks of the pure components was observed, implying their bonding together.

3.1.3. ZP. The charges on the surface of the $\text{FeS}_{0.5}/\text{MIL-88A}_{0.5}/\text{Cit-gCN}$ catalyst were measured by the ZP technique, as presented in Fig. 1c. The ZP findings demonstrate that the average charges on $\text{FeS}_{0.5}/\text{MIL-88A}_{0.5}/\text{Cit-gCN}$ at the pH values of 3, 5, 7, 9, and 11 are 7.22, 1.89, -11.29 , -26.22 , and -29.99 mV, respectively. It is concluded from the ZP curve that the $\text{FeS}_{0.5}/\text{MIL-88A}_{0.5}/\text{Cit-gCN}$ catalyst has no charge at pH = 5.29. $\text{FeS}_{0.5}/\text{MIL-88A}_{0.5}/\text{Cit-gCN}$ carries negative charges on its surface at a pH higher than 5.29; on the contrary, the surface charge of the catalyst becomes positive at a pH lower than 5.29.

3.1.4. SEM. The outer morphologies of FeS, MIL-88A, gCN, Cit-gCN, and $\text{FeS}_{0.5}/\text{MIL-88A}_{0.5}/\text{Cit-gCN}$ were scrutinized from the SEM images, as shown in Fig. 2a–e. For the gCN morphology, SEM elucidates the stacking of crumpled sheets with grooves and rough surfaces, endowing it with the characteristics of the excellent supporter. For the Cit-gCN morphology, the Cit particles are distributed on gCN sheets, confirming the Cit functionality, and this decoration likely increases the intersheet spacing and porosity, with an expected increase in its surface area. For the MIL-88A morphology, SEM reveals the common rod-like structure of the MIL-88A fabricated in aqueous media *via* the hydrothermal method. For the FeS morphology, SEM shows a flower-like morphology, which usually offers a large external surface and pore volume. For $\text{FeS}_{0.5}/\text{MIL-88A}_{0.5}/\text{Cit-gCN}$, the SEM image shows the uniform coverage of Cit-gCN sheets with the FeS and MIL-88A particles, which is expected to enhance the total pore volume and surface area. As a result, this combination is expected to provide a high surface area, which is the main factor in any efficient surface interaction.

3.1.5. XPS. The elemental composition of $\text{FeS}_{0.5}/\text{MIL-88A}_{0.5}/\text{Cit-gCN}$ was investigated by the XPS tool, as illustrated

in Fig. 3a–f. The XPS spectrum of $\text{FeS}_{0.5}/\text{MIL-88A}_{0.5}/\text{Cit-gCN}$ presents the peaks belonging to carbon, nitrogen, oxygen, iron, and sulfur at 286.07, 400.93, 532.45, 712.45, and 164.83 eV, and their atomic percents in the composite are 53.23%, 12.81%, 27.97%, 2.94%, and 3.05%, respectively. In the carbon spectrum, the peaks corresponding to $\text{N}=\text{C}-\text{N}$, $\text{C}-\text{C}$, and $\text{C}=\text{O}$ are revealed at 288.76, 284.47, and 285.71 eV, with atomic percents of 35.03%, 44.43%, and 20.53%, respectively. In the oxygen spectrum, the characteristic Fe–O peak (79.86%) of MIL-88A is observed at 531.34 eV, and the hydroxyl peak (20.14%) is observed at 533.11 eV. In the nitrogen spectrum, the peaks related to $\text{C}-\text{N}=\text{C}$ and $\text{C}-\text{N}$ are manifested at 400.29 and 399.03 eV, with atomic percents of 73.10% and 26.90%, respectively. In the sulfur spectrum, the Fe–S peak (4.74%), accompanying the iron sulfide, appears at 166.99 eV, and the peak at a binding energy of 168.42 eV represents the S–O bond (16.28%).³¹ In addition, the peak associated with the S–S bond emerges at 163.67 eV, with a total atomic percent of 78.98%.⁴⁵ In the iron spectrum, the peaks at 715.08 and 727.85 eV signalize the ferric species, while the ferrous species peaks are manifested at 711.28 and 724.37 eV. Furthermore, the net atomic percents of ferric and ferrous species in the $\text{FeS}_{0.5}/\text{MIL-88A}_{0.5}/\text{Cit-gCN}$ composites are 25.29% and 56.55%, respectively.

3.2. Optimization of the Fenton-like decomposition of Dox

3.2.1. Optimizing the composite's ratio. A sequence of adsorption/Fenton-like experiments for decomposing the Dox molecules by gCN, Cit-gCN, FeS, MIL-88A, and $\text{FeS}_{0.5}/\text{MIL-88A}_{0.5}/\text{Cit-gCN}$ was conducted to determine the improvement in the catalytic activity of gCN, as shown in Fig. 4a. The adsorption% and decomposition% of Dox by gCN were 13.28% and 48.92%, respectively, indicating its low catalytic activity, which requires enhancement. Surprisingly, the Cit functionality revealed an amelioration in the catalytic activity of gCN because the adsorption% and decomposition% of Dox reached 29.44% and 76.33%, respectively. This enhancement can be assigned to electron-rich groups in Cit that share their electrons for

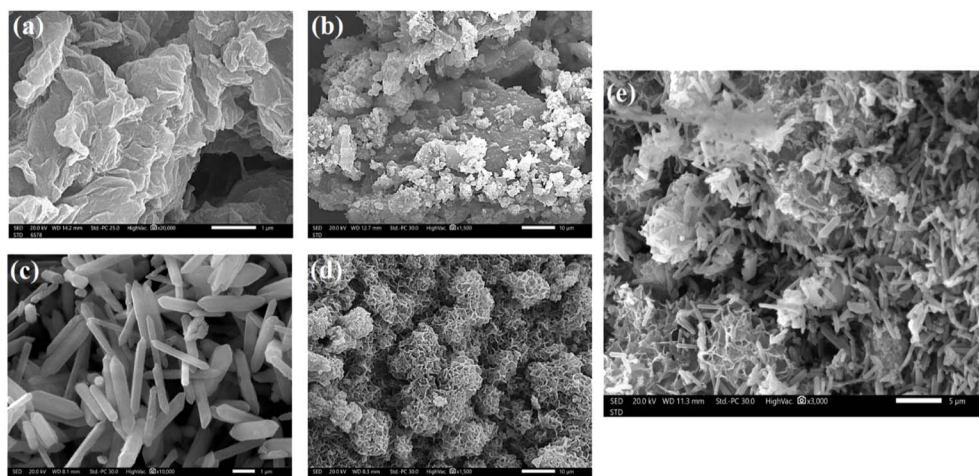


Fig. 2 SEM images of (a) gCN, (b) Cit-gCN, (c) MIL-88A, (d) FeS, and (e) $\text{FeS}_{0.5}/\text{MIL-88A}_{0.5}/\text{Cit-gCN}$.



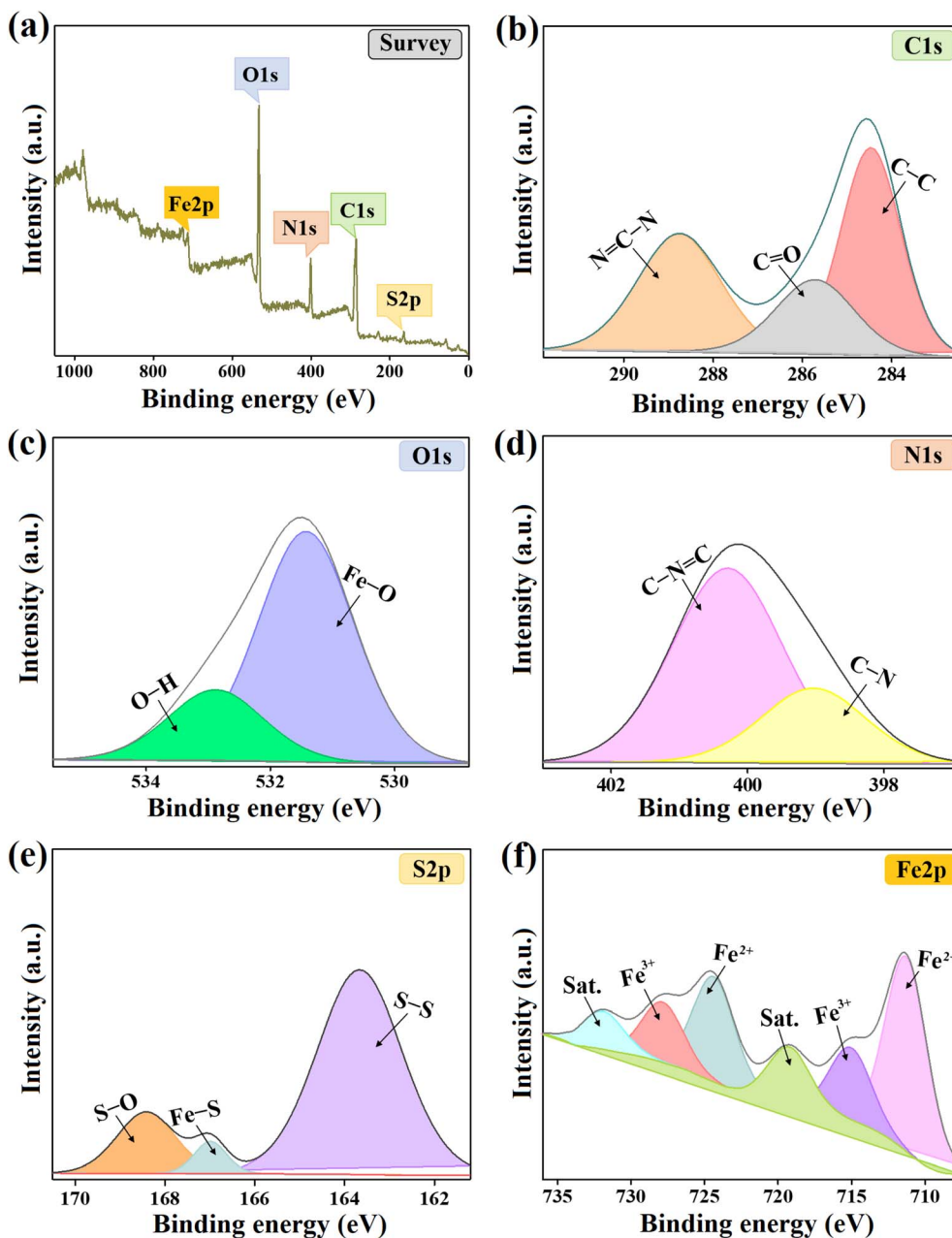


Fig. 3 XPS spectra of pure $\text{FeS}_{0.5}/\text{MIL-88A}_{0.5}@\text{Cit-gCN}$: (a) wide spectrum and (b) C 1s, (c) O 1s, (d) N 1s, (e) S 2p, and (f) Fe 2p spectra.

activating H_2O_2 and producing $\cdot\text{OH}$. Furthermore, the Cit modification increased the gCN' surface area, elevating its interaction with Dox. Moreover, the adsorption efficacies of FeS and MIL-88A toward Dox were 17.46% and 24.39%, and their decomposition percentages were 60.46% and 67.10%, respectively. Consequently, it was expected that binding FeS and MIL-88A with Cit-gCN could boost the composite's adsorption/catalytic activity by increasing its surface area as well as introducing active iron species and sulfur atoms from FeS. Likewise, MIL-88A has catalytic active groups like oxygenated functional groups and iron ions. These active species possess a high capacity for activating H_2O_2 and producing $\cdot\text{OH}$. As a result, the $\text{FeS}/\text{MIL-88A}@\text{Cit-gCN}$ composites exhibited an enhanced

catalytic activity toward decomposing Dox compared to the pure components, where $\text{FeS}_{0.5}/\text{MIL-88A}_{0.5}@\text{Cit-gCN}$ revealed a higher adsorption% of 48.77% and decomposition% of 94.66%, reflecting the synergistic effect between FeS, MIL-88A, and Cit-gCN.

3.2.2. Optimizing the pH medium. The best pH medium to decompose Dox by $\text{FeS}_{0.5}/\text{MIL-88A}_{0.5}@\text{Cit-gCN}$ with high efficiency was selected after testing the Fenton-like process at various pH values ranging from 3 to 11. The decomposition% vs. pH curve (Fig. 4b) signalizes the favorability of pH 5, where the adsorption% is 48.77%, and the Fenton-like decomposition% is 94.66%. Dox is one of the amphoteric drugs with a zwitter character at pH between 3.5 and 7.07, and it



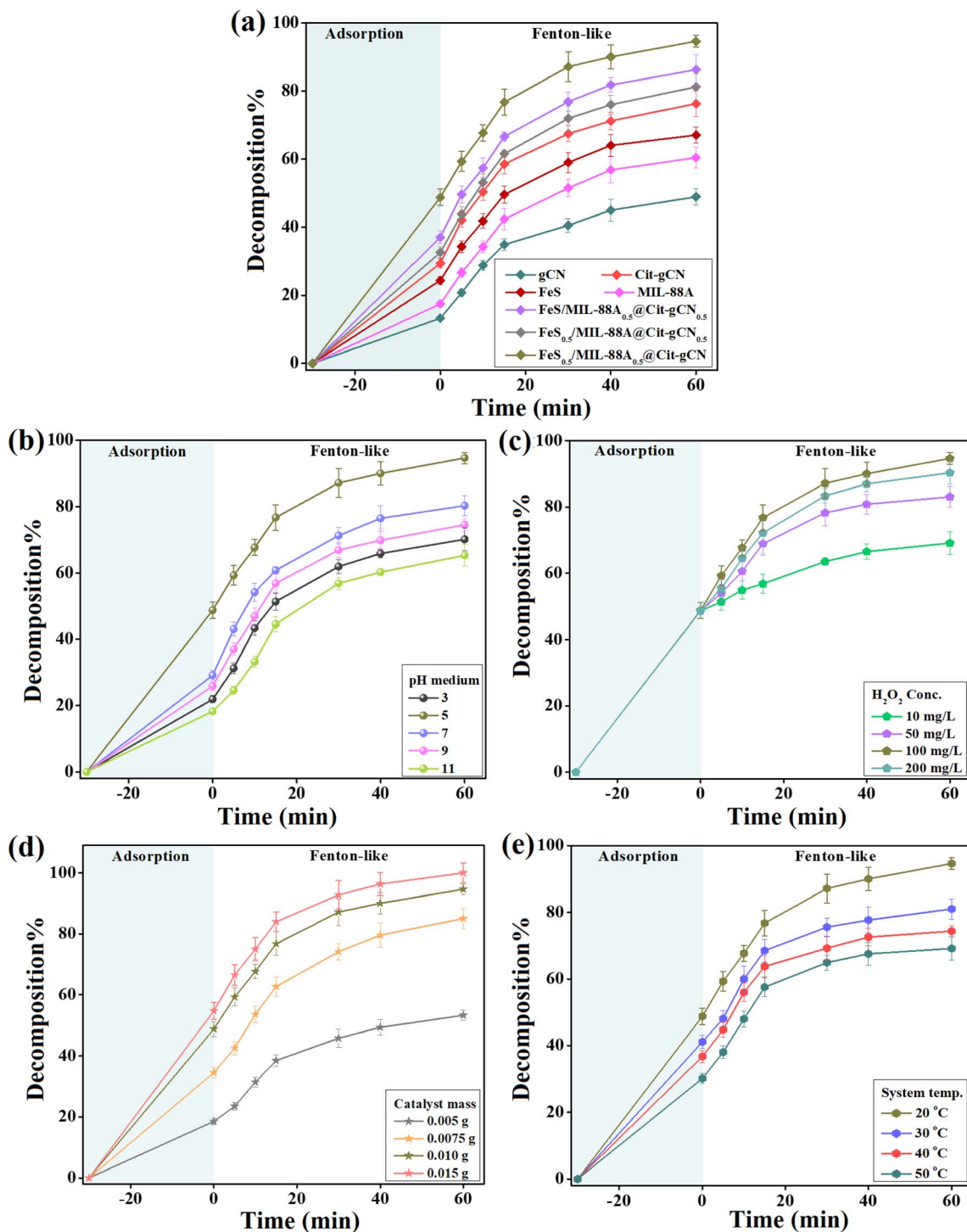


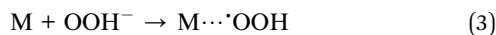
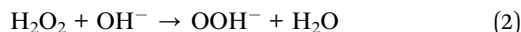
Fig. 4 Experimental results of the adsorption/Fenton-like decomposition of Dox by the FeS_{0.5}/MIL-88A_{0.5}@Cit-gCN composite: (a) comparison between the catalytic activity of the composites and pure components toward decomposing Dox, and optimization tests showing the effect of the (b) pH medium, (c) H₂O₂ concentration, (d) FeS_{0.5}/MIL-88A_{0.5}@Cit-gCN dose, and (e) system temperature on the decomposition% of Dox.

is a cation at pH < 3.5 and an anion at pH > 7.07. The FeS_{0.5}/MIL-88A_{0.5}@Cit-gCN composite has a neutral character at pH = 5.29, which increases the electrostatic interaction with the zwitter Dox. This observation endows merit to FeS_{0.5}/MIL-88A_{0.5}@Cit-gCN because the electrostatic repulsion is the obstacle to the adsorption process of such an amphoteric drug.

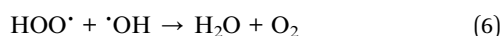
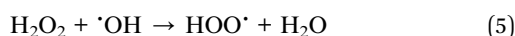
Furthermore, the excess hydroxyl groups in neutral and basic media may be the cause of the declining Fenton-like decomposition of Dox at a pH higher than 5 because they interact with H₂O₂ and produce hydro-peroxy anions, which attack the metal ions in the Dox/FeS_{0.5}/MIL-88A_{0.5}@Cit-gCN system, as clarified in eqn (2) and (3). Additionally, the self-decomposition of H₂O₂



degrades it into water and carbon dioxide, dwindling the produced concentration of $\cdot\text{OH}$ radicals, as shown in eqn (4).



3.2.3. Optimizing the H_2O_2 concentration. Fig. 4c displays the decomposition efficacy of Dox by $\text{FeS}_{0.5}/\text{MIL-88A}_{0.5}/\text{Cit-gCN}$ in the presence of various concentrations of H_2O_2 . It was recorded that raising the concentrations of the H_2O_2 molecules from 10 to 100 mg L^{-1} in the Dox- $\text{FeS}_{0.5}/\text{MIL-88A}_{0.5}/\text{Cit-gCN}$ system boosted the decomposition% of Dox from 69.15% to 94.66%, but further increasing it to 200 mg L^{-1} declined the percent of decomposed Dox to 90.33%. This catalytic performance could be ascribed to the fostered production of the $\cdot\text{OH}$ radicals by the elevated concentration of the H_2O_2 oxidant. Furthermore, excess concentrations of H_2O_2 in the Dox- $\text{FeS}_{0.5}/\text{MIL-88A}_{0.5}/\text{Cit-gCN}$ system could chelate the $\cdot\text{OH}$ radicals and create $\cdot\text{OOH}$, as elucidated in eqn (5) and (6).



3.2.4. Optimizing the $\text{FeS}_{0.5}/\text{MIL-88A}_{0.5}/\text{Cit-gCN}$ dosage. To determine the economical dosage to decompose the Dox molecules from wastewater with high efficiency, the $\text{FeS}_{0.5}/\text{MIL-88A}_{0.5}/\text{Cit-gCN}$ dosage was optimized, as presented in Fig. 4d. It was recorded that the adsorption% of Dox dramatically improved from 18.50% to 48.77% by elevating the $\text{FeS}_{0.5}/\text{MIL-88A}_{0.5}/\text{Cit-gCN}$ dosage from 0.005 g to 0.01 g, but further raising the dosage to 0.015 g caused an increase of only 6%. This result can be explained by the high concentrations of the provided active adsorption groups that chelate the Dox molecules from the polluted water. Likewise, the Dox decomposition% almost doubled when the $\text{FeS}_{0.5}/\text{MIL-88A}_{0.5}/\text{Cit-gCN}$ dosage increased from 0.005 to 0.01 g, but further increasing the $\text{FeS}_{0.5}/\text{MIL-88A}_{0.5}/\text{Cit-gCN}$ dose to 0.015 g did not reveal a significant effect. This catalytic behavior may be due to the enrichment of the system with highly active groups when the $\text{FeS}_{0.5}/\text{MIL-88A}_{0.5}/\text{Cit-gCN}$ dosage is 0.01 g, which can produce higher amounts of $\cdot\text{OH}$, decomposing higher concentrations of Dox molecules.³⁵ Consequently, 0.01 g is the optimal $\text{FeS}_{0.5}/\text{MIL-88A}_{0.5}/\text{Cit-gCN}$ dose, taking into consideration the economic point of view.

3.2.5. Optimizing the system temperature. Fig. 4e displays the decomposition% of Dox by $\text{FeS}_{0.5}/\text{MIL-88A}_{0.5}/\text{Cit-gCN}$ at increasing temperatures from room temperature to 50 $^\circ\text{C}$. The adsorption% of Dox diminished from 48.77% to 30.18%; in addition, the Dox decomposition% declined from 94.66% to 69.1%. Such a decrease in the decomposition efficiency of Dox occurs with raising the system temperature since the Brownian motion of Dox inside the catalytic system becomes faster,

diminishing the number of Dox molecules that reaches the $\text{FeS}_{0.5}/\text{MIL-88A}_{0.5}/\text{Cit-gCN}$ surface.⁴⁶

From the adsorption/Fenton-like optimization experiments, we deduced that the best mass ratio for FeS, MIL-88A, and Cit-gCN was 1 : 1 : 2. In addition, the optimal catalytic parameters for the decomposition process of Dox were system temperature = 20 $^\circ\text{C}$, pH = 5, $\text{FeS}_{0.5}/\text{MIL-88A}_{0.5}/\text{Cit-gCN}$ dose = 0.01 g, and H_2O_2 concentration = 100 mg L^{-1} .

3.3. Kinetic study

The catalytic activity of the Fenton-like $\text{FeS}_{0.5}/\text{MIL-88A}_{0.5}/\text{Cit-gCN}$ catalyst was investigated toward Dox at concentrations between 50 and 300 mg L^{-1} . As illustrated in Fig. 5a, the Dox adsorption% on the $\text{FeS}_{0.5}/\text{MIL-88A}_{0.5}/\text{Cit-gCN}$ surface declined from 48.77% to 20.27% as the Dox concentration increased from 50 to 300 mg L^{-1} . Meanwhile, the increase in the Dox concentrations diminished the decomposition% of Dox from 99.40% to 66.27%. These findings can be explained by the insufficient amount of active groups on the $\text{FeS}_{0.5}/\text{MIL-88A}_{0.5}/\text{Cit-gCN}$ surface to adsorb and produce enough $\cdot\text{OH}$ to decompose the higher concentrations of Dox.³⁵

The kinetics of the decomposition process of Dox by $\text{FeS}_{0.5}/\text{MIL-88A}_{0.5}/\text{Cit-gCN}$ was inspected by the catalytic first-order and second-order models (eqn (7) and (8), respectively).

$$\ln \frac{C_t}{C_0} = -k_1 t \quad (7)$$

$$\frac{1}{C_t} = \frac{1}{C_0} + k_2 t \quad (8)$$

where k_1 and k_2 are the rate constants of the first-order and second-order models, respectively.

As revealed in Table 1, the decomposition reaction of Dox by $\text{FeS}_{0.5}/\text{MIL-88A}_{0.5}/\text{Cit-gCN}$ obeyed the second-order kinetic expression, and the correlation coefficients of the linear second-order plot were higher than those of the first-order plot (Fig. 5b and c). The rate constants of the decomposition reaction of 50, 100, 200, and 300 mg L^{-1} Dox by $\text{FeS}_{0.5}/\text{MIL-88A}_{0.5}/\text{Cit-gCN}$ decreased from 0.4260 to 0.0485, 0.0232, and 0.0127 $\text{L mol}^{-1} \text{min}^{-1}$, respectively. This observation is most likely due to the complex interplay of catalytic parameters in the decomposition reaction, such as the simultaneous production and consumption of $\cdot\text{OH}$ radicals. Furthermore, compounds formed during the decomposition of Dox could compete with Dox molecules within the catalytic system.^{47–49}

3.4. Adsorption/Fenton-like mechanisms

To determine the type of catalytic decomposition mechanism for Dox by $\text{FeS}_{0.5}/\text{MIL-88A}_{0.5}/\text{Cit-gCN}$, the scavenging test was performed in the presence of TCM and *t*-BuOH, separately, as illustrated in Fig. 6a. TCM and *t*-BuOH are the common scavengers used to explore the domination of the active $\text{O}_2^{\cdot-}$ and $\cdot\text{OH}$ radicals, respectively, in the catalytic media owing to their ability to slow down the activity of these radicals.⁵⁰ The experimental observations signalize the diminution in the decomposition capability of $\text{FeS}_{0.5}/\text{MIL-88A}_{0.5}/\text{Cit-gCN}$ toward Dox,



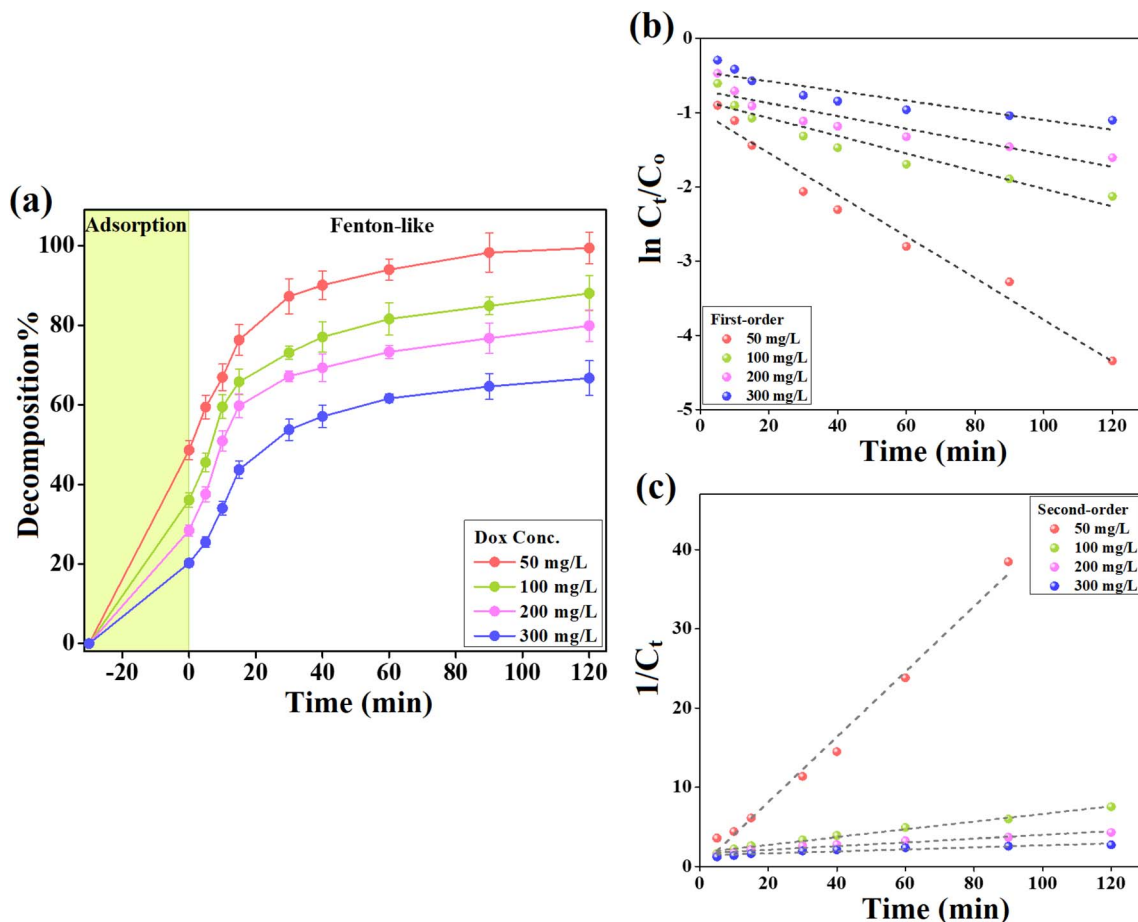


Fig. 5 (a) Catalytic activity of $\text{FeS}_{0.5}/\text{MIL-88A}_{0.5}@\text{Cit-gCN}$ toward decomposing various Dox concentrations, and kinetic analysis of the Fenton-like decomposition of Dox: (b) first-order and (c) second-order plots.

Table 1 Parameters derived from the kinetic study of the Fenton-like decomposition of Dox by $\text{FeS}_{0.5}/\text{MIL-88A}_{0.5}@\text{Cit-gCN}$

Kinetic model	Dox concentrations (mg L^{-1})			
	50	100	200	300
First-order				
k_1	0.0281	0.0119	0.0086	0.0065
R^2	0.968	0.909	0.847	0.818
Second-order				
k_2	0.4260	0.0485	0.0232	0.0127
R^2	0.992	0.990	0.946	0.889

reaching 69.39%, in the presence of *t*-BuOH, implying that $\cdot\text{OH}$ is the active radical in the Dox- $\text{FeS}_{0.5}/\text{MIL-88A}_{0.5}@\text{Cit-gCN}$ system.⁵¹ Consequently, the catalytic decomposition reaction of Dox by $\text{FeS}_{0.5}/\text{MIL-88A}_{0.5}@\text{Cit-gCN}$ occurs throughout the radical pathway mechanism.

XPS spectra signalizes the production process of $\cdot\text{OH}$ in the Fenton-like catalytic Dox- $\text{FeS}_{0.5}/\text{MIL-88A}_{0.5}@\text{Cit-gCN}$ system, as clarified below:

(i) The iron species are the typical active species in activating H_2O_2 and yielding $\cdot\text{OH}$, following the catalytic Haber-Weiss

process (eqn (9)). Notably, the iron species in $\text{FeS}_{0.5}/\text{MIL-88A}_{0.5}@\text{Cit-gCN}$ are divided into 56.55% of Fe^{2+} and 25.29% of Fe^{3+} with a $\text{Fe}^{3+}/\text{Fe}^{2+}$ ratio of 0.447. By contrast, the XPS spectrum of the used $\text{FeS}_{0.5}/\text{MIL-88A}_{0.5}@\text{Cit-gCN}$ reveals an elevation in the $\text{Fe}^{3+}/\text{Fe}^{2+}$ ratio to 0.852, suggesting the consumption of a part of Fe^{2+} during the Fenton-like decomposition of Dox in the production reaction of $\cdot\text{OH}$ (Fig. 6b). Moreover, the shifting in the iron peaks is another clue confirming its role in the Fenton-like decomposition of Dox; the Fe^{2+} peaks shift from 711.28 and 724.37 eV to 710.94 and 723.71 eV, and the position of the Fe^{3+} peaks changes from 715.08 and 727.85 eV to 714.57 and 727.44 eV, respectively.

(ii) The sulfur species in the $\text{FeS}_{0.5}/\text{MIL-88A}_{0.5}@\text{Cit-gCN}$ catalyst can foster the catalytic activity of the near-iron species by presenting defects and transferring electrons from the Fe-S bond to the catalyst. Therefore, the unsaturated sulfur ions increase the shared electrons from $\text{FeS}_{0.5}/\text{MIL-88A}_{0.5}@\text{Cit-gCN}$ to activate H_2O_2 and create $\cdot\text{OH}$. The sulfur spectrum of the $\text{FeS}_{0.5}/\text{MIL-88A}_{0.5}@\text{Cit-gCN}$ catalyst after the Dox decomposition (Fig. 6c) clarifies changes in the position of the sulfur peaks; Fe-S, S-O, and S-S peaks shift from 166.99, 168.42, and 163.67 eV to 168.40, 169.95, and 163.31 eV, respectively, proving its contribution in the H_2O_2 activation.



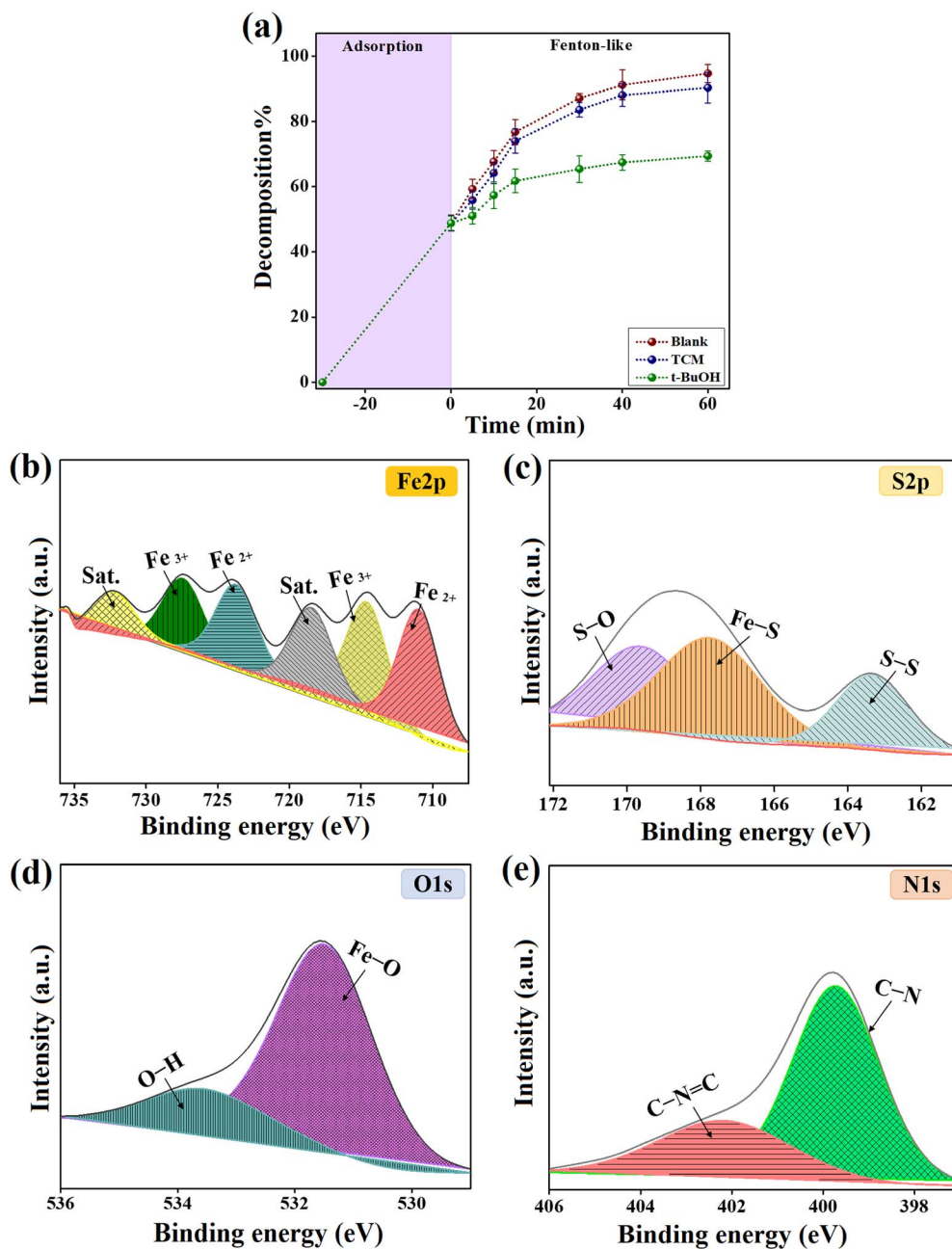


Fig. 6 (a) Quenching test of the decomposition process of Dox by $\text{FeS}_{0.5}/\text{MIL-88A}_{0.5}@\text{Cit-gCN}$ and XPS spectra of used $\text{FeS}_{0.5}/\text{MIL-88A}_{0.5}@\text{Cit-gCN}$: (b) Fe 2p, (c) S 2p, (d) O 1s, and (e) N 1s.

(iii) The $\text{FeS}_{0.5}/\text{MIL-88A}_{0.5}@\text{Cit-gCN}$ catalyst possesses many electron-donating groups, like hydroxyl, tri-*s*-triazine, and carboxyl, which can participate in the Fenton-like decomposition of Dox by donating electrons to the catalytic medium for producing $\cdot\text{OH}$, as presented in eqn (10). Moreover, such groups can regenerate the oxidized iron species to reuse them in the decomposition process of the Dox molecules (eqn (11)). Hence, the electron-donor groups of $\text{FeS}_{0.5}/\text{MIL-88A}_{0.5}@\text{Cit-gCN}$ can initiate the decomposition process of Dox and maintain the continuity of the $\text{Fe}^{3+}/\text{Fe}^{2+}$ redox cycle. Fig. 6d displays a variation in the positions of the Fe–O and hydroxyl peaks of the used $\text{FeS}_{0.5}/\text{MIL-88A}_{0.5}@\text{Cit-gCN}$ catalyst from 531.34 and 533.11 eV

to 531.47 and 533.60 eV, respectively. Also, the peaks of the nitrogen-containing functional groups C–N=C and C–N shift from 400.29 and 399.03 eV to 402.20 and 399.72 eV, respectively, as illustrated in Fig. 6e. These observations ensure the involvement of the hydroxyl, tri-*s*-triazine, and carboxyl groups in the decomposition reaction of the Dox molecules.

Shortly, the iron, sulfur, hydroxyl, tri-*s*-triazine, and carboxyl species of $\text{FeS}_{0.5}/\text{MIL-88A}_{0.5}@\text{Cit-gCN}$ activate H_2O_2 and produce $\cdot\text{OH}$, which decomposes the Dox molecules to smaller compounds, resulting in the formation of CO_2 and H_2O , as clarified in eqn (12).



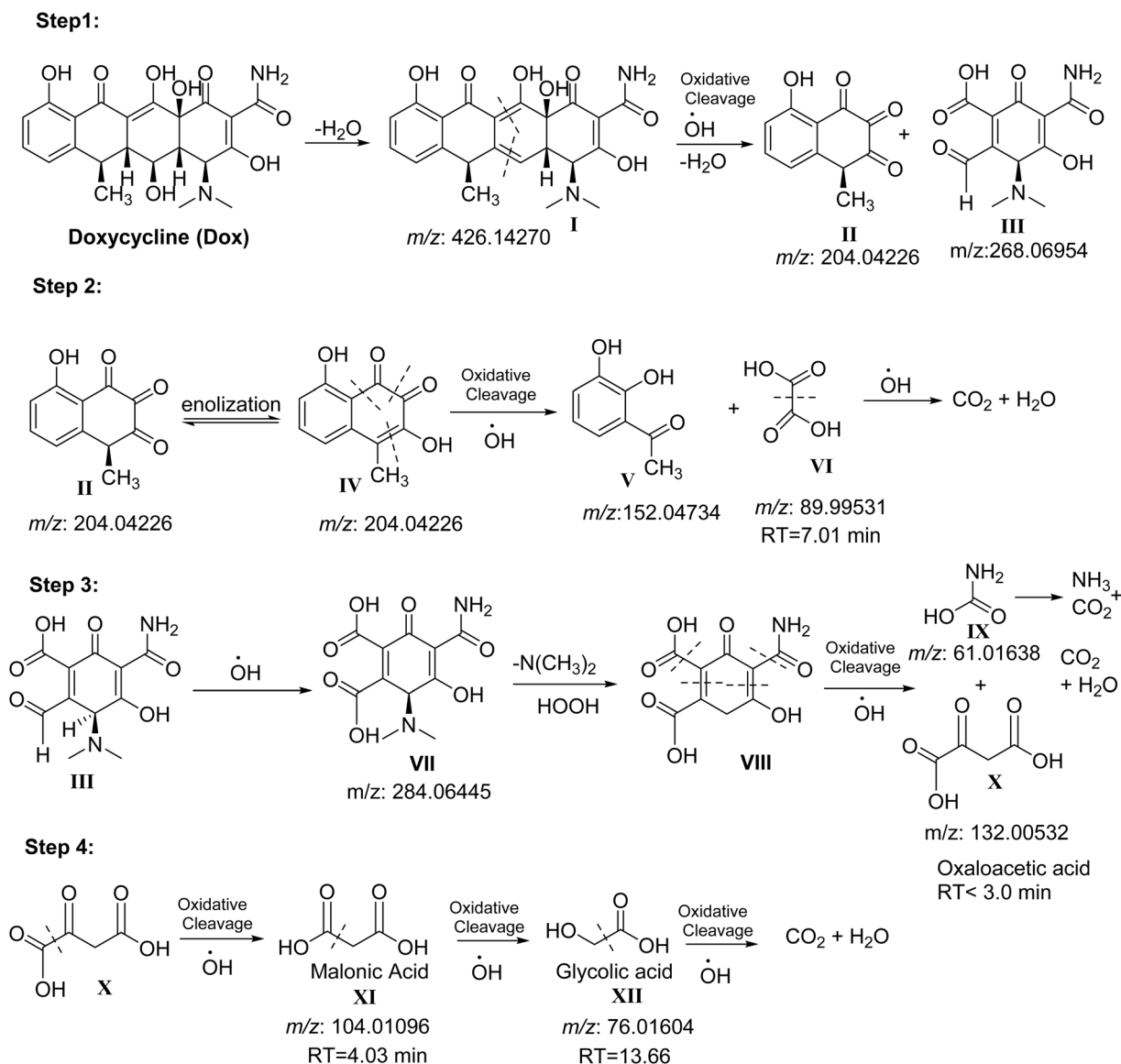
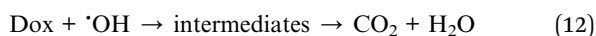
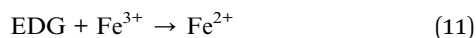
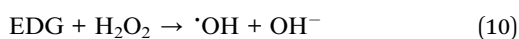
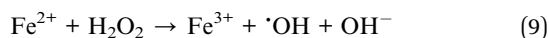


Fig. 7 Schematic of the adsorption/Fenton-like decomposition of Dox by $\text{FeS}_{0.5}/\text{MIL-88A}_{0.5}/\text{Cit-gCN}$.



Notably, the experimental results reveal the significant role of the adsorption reaction in the capacity of the Dox decomposition; so, it is important to suggest the mechanism of adsorbing Dox onto $\text{FeS}_{0.5}/\text{MIL-88A}_{0.5}/\text{Cit-gCN}$, as follows: (i) Dox can adsorb onto $\text{FeS}_{0.5}/\text{MIL-88A}_{0.5}/\text{Cit-gCN}$ via the coulombic interaction between the zwitter Dox and the zwitter catalyst at pH ~ 5 . The presence of $\text{FeS}_{0.5}/\text{MIL-88A}_{0.5}/\text{Cit-gCN}$ in a zwitter state at the same pH at which the amphoteric Dox exists in its zwitter character grants the catalyst a special merit

because it overcomes the possible repulsion forces that are usually generated during the adsorption reaction of such amphoteric drugs and decline their adsorption capacity.

(ii) The iron species not only activate H_2O_2 to create $\cdot\text{OH}$, but also play a worthy role during the adsorption reaction, where they can attach to the electron-donor groups of Dox (*viz.*, hydroxyl and amine) throughout coordination bonds.^{52,53} Furthermore, the presence of nitrogen and oxygen atoms in both $\text{FeS}_{0.5}/\text{MIL-88A}_{0.5}/\text{Cit-gCN}$ and Dox suggests the H-bonding between the N and O of Dox and the H of the catalyst. In addition, there is a possibility of the N and O of $\text{FeS}_{0.5}/\text{MIL-88A}_{0.5}/\text{Cit-gCN}$ chelating Dox by forming H-bonds with its H atoms.

(iii) n-pi interactions are a governing pathway in the adsorption reaction of Dox because its empty pi-orbital is available to accept electrons from the catalyst. The $\text{FeS}_{0.5}/\text{MIL-88A}_{0.5}/\text{Cit-gCN}$ catalyst is rich with electron-donor active



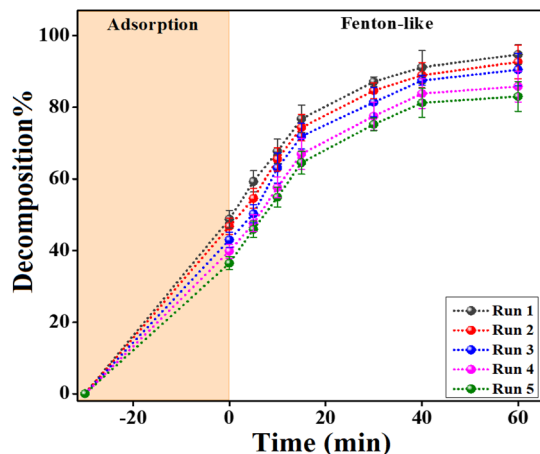


Fig. 8 Cycling study of the $\text{FeS}_{0.5}/\text{MIL-88A}_{0.5}@\text{Cit-gCN}$ catalyst during five decomposition runs of Dox.

groups, comprising OH, tri-*s*-triazine, and COOH that share electrons with the empty pi-orbital of Dox; so, the catalyst can adsorb the Dox molecules onto its surface by forming n- π interactions.⁵⁴

3.5. Decomposition pathway

The degradation pathway of Dox by $\text{FeS}_{0.5}/\text{MIL-88A}_{0.5}@\text{Cit-gCN}$ was suggested, based on the GC-MS and retention time results, as illustrated in Fig. S1. The degradation pathway includes 4 steps, as illustrated in Fig. 7. In the first step, Dox loses one molecule of water to afford the conjugated diene **I** with an experimentally identified mass of $m/z = 425.3$, which agrees with the calculated mass of $[M - H] = 425.1$, with **I** undergoing oxidative cleavage by $\cdot\text{OH}$ radicals to afford the corresponding key fragments (**II** and **III**). The degradation of the fragment (**II**) occurs in step 2 *via* enolization to afford **IV**, which decomposes by oxidative cleavage to afford acetyl catechol (**V**) and oxalic acid (**VI**). This pathway is confirmed by the result of GC-MS, where the RT of oxalic acid is 7.01, which agrees with the reported value in the literature and the mass of $m/z = 91.2$ corresponding to $[M + 2H]$. The decomposition of oxalic acid finally gives CO_2 and water. The third step includes the degradation of the key compound, the reactive fragment **III**, which oxidizes rapidly to the corresponding acid (**VII**) and then loses dimethylamine, followed by hydrogen radical transfer to give (**VIII**). **VIII** is decomposed *via* oxidation to give the unstable carbamic acid (**IX**) and oxaloacetic acid (**X**). Carbamic acid degrades directly to ammonia and CO_2 . Oxaloacetic acid (**X**) has a low RT, less than 3.0 min, because its stability is limited. Experimental m/z of the oxaloacetic acid (**X**) = 134.5 which agree with the theoretical m/z value of the corresponding $[M + 2H]$. In the last step, the decarboxylation of **X** affords malonic acid **XI** with an RT of 4.03 min, which oxidizes to glycolic acid **XII** with RT = 13.66 min, agreeing with the reported value in the literature.^{55,56}

3.6. Recycling investigation

The durability and reusability of the Fenton-like $\text{FeS}_{0.5}/\text{MIL-88A}_{0.5}@\text{Cit-gCN}$ catalyst are essential criteria that must be met

before recommending its use on an industrial scale. Therefore, the adsorption/Fenton-like cycling test was performed on the $\text{FeS}_{0.5}/\text{MIL-88A}_{0.5}@\text{Cit-gCN}$ catalyst for five runs to investigate the capability of its recyclability feature. The cycling curve in Fig. 8 displays an insignificant decline in the adsorption% and decomposition% of Dox by $\text{FeS}_{0.5}/\text{MIL-88A}_{0.5}@\text{Cit-gCN}$ by about 12.29% and 11.64%, respectively. Such a diminution in the adsorption% of Dox can be ascribed to the potent chemical and physical interactions between Dox and $\text{FeS}_{0.5}/\text{MIL-88A}_{0.5}@\text{Cit-gCN}$ that hinder the complete desorption of the Dox particles during the recovery stage. Consequently, the adsorbed Dox on the active sites of $\text{FeS}_{0.5}/\text{MIL-88A}_{0.5}@\text{Cit-gCN}$ shields those active groups and prevents them from donating electrons for activating H_2O_2 . In addition, some mass of $\text{FeS}_{0.5}/\text{MIL-88A}_{0.5}@\text{Cit-gCN}$ can be lost during the washing step of the catalyst recovery process.

4. Conclusion

The Fenton-like heterogeneous $\text{FeS}_{0.5}/\text{MIL-88A}_{0.5}@\text{Cit-gCN}$ catalyst revealed an eminent catalytic activity towards decomposing Dox, where the adsorption% was 48.78% after half an hour and the decomposition% was 99.40% after two hours at pH = 5, temperature = 20 °C, and H_2O_2 concentration = 100 mg L^{-1} . The zeta potential results implied that the zero charge point of $\text{FeS}_{0.5}/\text{MIL-88A}_{0.5}@\text{Cit-gCN}$ was at pH = 5.29, endowing the catalyst an advantage because it overcame the electrostatic repulsion problem that hinders the adsorption of amphoteric Dox. Furthermore, the SEM of $\text{FeS}_{0.5}/\text{MIL-88A}_{0.5}@\text{Cit-gCN}$ elucidated the presence of FeS and MIL-88A on the surface of Cit-gCN. The XPS spectra of used/genuine $\text{FeS}_{0.5}/\text{MIL-88A}_{0.5}@\text{Cit-gCN}$ depicted the participation of its iron, sulfur, and electron-donor groups in activating H_2O_2 and creating $\cdot\text{OH}$ for decomposing Dox. In addition, the adsorption of Dox onto $\text{FeS}_{0.5}/\text{MIL-88A}_{0.5}@\text{Cit-gCN}$ occurred through n- π interactions, coulombic interactions, and coordination bonds. The recycling study showed a slight decrease in the activity during $\text{FeS}_{0.5}/\text{MIL-88A}_{0.5}@\text{Cit-gCN}$ adsorption/Fenton-like decomposition cycles of Dox.

Future studies are recommended to expand the redox cycle by incorporating additional metal species through metal doping or by integrating metal-rich materials such as layered double hydroxides, MXenes, metal ferrites/oxides, or MOFs into the composite structure. Furthermore, the decline in the activity of $\text{FeS}_{0.5}/\text{MIL-88A}_{0.5}@\text{Cit-gCN}$ during its recycling and reuse during Dox decomposition may be attributed to mass loss; so, adding magnetic materials to the composite or encapsulating it inside a polymeric matrix in a bead shape may be a suitable solution to this bottleneck. Moreover, a comprehensive study of composite surface characteristics will provide deeper insights into the surface-related phenomena governing catalytic performance.

Conflicts of interest

There are no conflicts to declare.



Data availability

The datasets supporting the findings of this study are available within the article and its supplementary information (SI) files. Supplementary information is available. See DOI: <https://doi.org/10.1039/d5ra07120h>.

Funding

This work was supported by the Deanship of Scientific Research, Vice Presidency for Graduate Studies and Scientific Research, King Faisal University, Saudi Arabia [Project No. KFU253362].

Acknowledgements

JA and MSA acknowledge the Deanship of Scientific Research, Vice Presidency for Graduate Studies and Scientific Research, King Faisal University, Saudi Arabia, for financial support under the annual funding track [KFU253362].

References

- M. Sodhi and M. Etminan, Therapeutic Potential for Tetracyclines in the Treatment of COVID-19, *Pharmacotherapy*, 2020, **40**(5), 487.
- J. A. Mosquera-Sulbaran and H. Hernández-Fonseca, Tetracycline and viruses: a possible treatment for COVID-19?, *Archives of virology*, 2021, **166**, 1–7.
- A. S. Eltaweil, *et al.*, Enhanced fenton degradation of tetracycline over cerium-doped MIL88-A/g-C3N4: Catalytic performance and mechanism, *Nanomaterials*, 2024, **14**(15), 1282.
- A. S. Eltaweil, *et al.*, Engineering of a wafer-shaped titanium-based catalyst of TiO₂/MIL-125 (Ti)@ Ti₃C₂ for enhanced Fenton-like degradation of Congo red: Optimization, mechanistic study, and reusability, *J. Ind. Eng. Chem.*, 2025, **143**, 704–716.
- E. M. Abd El-Monaem, *et al.*, Harnessing the storage-release cavity of β -cyclodextrin to enhance SnFe₂O₄/FeCoNi-LTH catalyst efficiency in fenton-like degradation of tetracycline, *Surf. Interfaces*, 2025, **58**, 105749.
- N. Wang, *et al.*, A review on Fenton-like processes for organic wastewater treatment, *J. Environ. Chem. Eng.*, 2016, **4**(1), 762–787.
- A. S. Eltaweil, *et al.*, Design of a magnetic Fenton-like catalyst by decorating diamond-shaped MIL-88A with Chenopodium-derived biochar for nitrophenol degradation: optimization and mechanistic insights, *RSC Adv.*, 2025, **15**(25), 20111–20124.
- E. M. Abd El-Monaem, *et al.*, Cyclodextrin Polymer-Embedded NiS/FeS Composite as a Fenton-like Catalyst for the Degradation of Cresol Red, *Polymers*, 2025, **17**(7), 876.
- S. Cao, *et al.*, Polymeric photocatalysts based on graphitic carbon nitride, *Adv. Mater.*, 2015, **27**(13), 2150–2176.
- Y. Zhang, *et al.*, Porous graphitic carbon nitride synthesized via direct polymerization of urea for efficient sunlight-driven photocatalytic hydrogen production, *Nanoscale*, 2012, **4**(17), 5300–5303.
- Q. Peng, Y. Dong and Y. Li, ZnSe semiconductor hollow microspheres, *Angew. Chem.*, 2003, **115**(26), 3135–3138.
- A. Thomas, *et al.*, Graphitic carbon nitride materials: variation of structure and morphology and their use as metal-free catalysts, *J. Mater. Chem.*, 2008, **18**(41), 4893–4908.
- C. Tian, *et al.*, Enhanced adsorption and photocatalytic activities of ultrathin graphitic carbon nitride nanosheets: Kinetics and mechanism, *Chem. Eng. J.*, 2020, **381**, 122760.
- G. Xiao, *et al.*, Superior adsorption performance of graphitic carbon nitride nanosheets for both cationic and anionic heavy metals from wastewater, *Chin. J. Chem. Eng.*, 2019, **27**(2), 305–313.
- M. A. Oturan, *et al.*, Reaction sequence for the mineralization of the short-chain carboxylic acids usually formed upon cleavage of aromatics during electrochemical Fenton treatment, *Electrochim. Acta*, 2008, **54**(2), 173–182.
- C. Kwan and W. Chu, The role of organic ligands in ferrous-induced photochemical degradation of 2, 4-dichlorophenoxyacetic acid, *Chemosphere*, 2007, **67**(8), 1601–1611.
- W. Jiang, *et al.*, Enhanced redox degradation of chlorinated hydrocarbons by the Fe (II)-catalyzed calcium peroxide system in the presence of formic acid and citric acid, *J. Hazard. Mater.*, 2019, **368**, 506–513.
- J. Bolobajev, M. Trapido and A. Goi, Improvement in iron activation ability of alachlor Fenton-like oxidation by ascorbic acid, *Chem. Eng. J.*, 2015, **281**, 566–574.
- K. H. Badagoppam Haroon and S. K. Bhunia, Fenton-like catalysts based on graphitic carbon nitride nanosheets decorated with Fe₃O₄ nanoparticles for removal of colorless tetracycline, *ACS Appl. Nano Mater.*, 2024, **7**(23), 26356–26368.
- X. Mu, *et al.*, Sustainable and energy-efficient degradation of acetaminophen in water using an optimized fenton-like system with iron-doped graphitic carbon nitride catalyst, *J. Environ. Chem. Eng.*, 2025, **13**(2), 115760.
- W. Liu, *et al.*, Facile synthesis of Z-scheme g-C₃N₄@ MIL-100 (Fe) and the efficient photocatalytic degradation on doxycycline and disinfection by-products by coupling with persulfate: Mechanism and pathway, *Colloids Surf., A*, 2022, **635**, 128057.
- E. M. Abd El-Monaem, A. M. Omer and A. S. Eltaweil, Durable and low-cost Chitosan decorated Fe/MOF-5 bimetallic MOF composite film for high performance of the Congo red adsorption, *J. Polym. Environ.*, 2024, **32**(5), 2075–2090.
- J. Tang and J. Wang, Metal organic framework with coordinatively unsaturated sites as efficient Fenton-like catalyst for enhanced degradation of sulfamethazine, *Environ. Sci. Technol.*, 2018, **52**(9), 5367–5377.
- V. P. Viswanathan, *et al.*, Exploring the effect of morphologies of Fe (III) metal-organic framework MIL-88A (Fe) on the photocatalytic degradation of rhodamine B, *ChemistrySelect*, 2020, **5**(25), 7534–7542.



- 25 H. Fu, *et al.*, Room-temperature preparation of MIL-88A as a heterogeneous photo-Fenton catalyst for degradation of rhodamine B and bisphenol a under visible light, *Mater. Res. Bull.*, 2020, **125**, 11806.
- 26 X. Liao, *et al.*, Synthesis of (100) surface oriented MIL-88A-Fe with rod-like structure and its enhanced fenton-like performance for phenol removal, *Appl. Catal., B*, 2019, **259**, 118064.
- 27 K.-Y. A. Lin, H.-A. Chang and C.-J. Hsu, Iron-based metal organic framework, MIL-88A, as a heterogeneous persulfate catalyst for decolorization of Rhodamine B in water, *RSC Adv.*, 2015, **5**(41), 32520–32530.
- 28 K.-X. Shi, *et al.*, Magnetic MgFe₂O₄/MIL-88A catalyst for photo-Fenton sulfamethoxazole decomposition under visible light, *Sep. Purif. Technol.*, 2022, **301**, 121965.
- 29 J.-S. Wang, *et al.*, Eliminating tetracycline antibiotics matrix via photoactivated sulfate radical-based advanced oxidation process over the immobilized MIL-88A: Batch and continuous experiments, *Chem. Eng. J.*, 2022, **431**, 133213.
- 30 A. S. Eltaweil, *et al.*, Enhanced fenton degradation of tetracycline over cerium-doped MIL88-A/g-C₃N₄: Catalytic performance and mechanism, *Nanomaterials*, 2024, **14**(15), 1282.
- 31 B. Wang, *et al.*, Dissolution reconstruction of electron-transfer enhanced hierarchical NiSx-MoO₂ nanosponges as a promising industrialized hydrogen evolution catalyst beyond Pt/C, *J. Colloid Interface Sci.*, 2020, **567**, 339–346.
- 32 R. Bai, *et al.*, Acceleration of peroxymonosulfate decomposition by a magnetic MoS₂/CuFe₂O₄ heterogeneous catalyst for rapid degradation of fluoxetine, *Chem. Eng. J.*, 2020, **397**, 125501.
- 33 A. M. Aljeboree, A. F. Alkaim and A. H. Al-Dujaili, Adsorption isotherm, kinetic modeling and thermodynamics of crystal violet dye on coconut husk-based activated carbon, *Desalin. Water Treat.*, 2015, **53**(13), 3656–3667.
- 34 F. Mashkoo, *et al.*, Exploring the reusability of synthetically contaminated wastewater containing crystal violet dye using tectona grandis sawdust as a very low-cost adsorbent, *Sci. Rep.*, 2018, **8**(1), 8314.
- 35 E. M. Abd El-Monaem, *et al.*, Enhanced redox cycle of rod-shaped MIL-88A/SnFe₂O₄@ MXene sheets for Fenton-like degradation of Congo Red: optimization and mechanism, *Nanomaterials*, 2023, **14**(1), 54.
- 36 Y. Yang, *et al.*, Two novel and efficient plant composites for the degradation of oxytetracycline: nanoscale ferrous sulphide supported on rape straw waste, *Environ. Sci. Pollut. Res.*, 2022, **29**(42), 63545–63559.
- 37 Y. Cai, J. Fan and Z. Liu, Enhanced degradation of tetracycline over FeS-based Fenton-like process: Autocatalytic decomposition of H₂O₂ and reduction of Fe (III), *J. Hazard. Mater.*, 2022, **436**, 129092.
- 38 S. Shit, *et al.*, Effect of the solvent ratio (ethylene glycol/water) on the preparation of an iron sulfide electrocatalyst and its activity towards overall water splitting, *ChemElectroChem*, 2019, **6**(12), 3199–3208.
- 39 X. Min, *et al.*, Fe-FeS₂ adsorbent prepared with iron powder and pyrite by facile ball milling and its application for arsenic removal, *Water Sci. Technol.*, 2017, **76**(1), 192–200.
- 40 M. A. Agoro and E. L. Meyer, FeS/FeS₂ nanoscale structures synthesized in one step from Fe (II) dithiocarbamate complexes as a single source precursor, *Front. Chem.*, 2022, **10**, 1035594.
- 41 B. Y. Danu, *et al.*, Iron sulfide functionalized polyaniline nanocomposite for the removal of Eosin Y from water: Equilibrium and kinetic studies, *Polym. Sci., Ser. B*, 2021, **63**(3), 304–313.
- 42 M. Chebanenko, *et al.*, Ultrasonic-assisted exfoliation of graphitic carbon nitride and its electrocatalytic performance in process of ethanol reforming, *Semiconductors*, 2019, **53**(16), 2072–2077.
- 43 S. Mallakpour and A. Nezamzadeh Ezhieh, Citric acid and vitamin C as coupling agents for the surface coating of ZrO₂ nanoparticles and their behavior on the optical, mechanical, and thermal properties of poly (vinyl alcohol) nanocomposite films, *J. Polym. Environ.*, 2018, **26**, 2813–2824.
- 44 M. Z. Mathew, *et al.*, The synthesis of FeS and investigation on electrochemical sensing toward neuroprotector, *Cureus*, 2024, **16**(4).
- 45 L. Yang, *et al.*, Hierarchical NiS₂ modified with bifunctional carbon for enhanced potassium-ion storage, *Adv. Funct. Mater.*, 2019, **29**(50), 1903454.
- 46 S. Rawat and J. Singh, Fenton like oxidative degradation of toxic water pollutants by iron nanoparticles synthesized via facile green route using waste iron rust as the iron precursor, *Environ. Eng. Res.*, 2023, **28**(2), 210621.
- 47 T. Geng, *et al.*, Efficient degradation of methylene blue at near neutral pH based on heterogeneous Fenton-like system catalyzed by Fe₂O₃/MnO₂, *Results Chem.*, 2024, **11**, 101795.
- 48 J. Singh, *et al.*, Fenton-Like degradation of methylene blue by ultrasonically dispersed nano zero-valent metals, *Environ. Processes*, 2017, **4**(1), 169–182.
- 49 M. Karim, *et al.*, Degradation of aqueous organic dye pollutants by heterogeneous photo-assisted Fenton-like process using natural mineral activator: Parameter optimization and degradation kinetics, *IOP Conference Series: Earth and Environmental Science*, IOP Publishing, 2021.
- 50 U. Farooq, *et al.*, Synthesis of nZVI@ reduced graphene oxide: an efficient catalyst for degradation of 1, 1, 1-trichloroethane (TCA) in percarbonate system, *Res. Chem. Intermed.*, 2017, **43**, 3219–3236.
- 51 S.-Q. Zhang, *et al.*, Constructing a Z-Scheme Co₃O₄/BiOBr Heterojunction to Enhance Photocatalytic Peroxydisulfate Oxidation of High-Concentration Rhodamine B: Mechanism, Degradation Pathways, and Toxicological Evaluations, *Inorg. Chem.*, 2024, **63**(9), 4447–4460.
- 52 X. Zhang, *et al.*, Precision grinding of silicon nitride ceramic with laser macro-structured diamond wheels, *Opt Laser Technol.*, 2019, **109**, 418–428.



- 53 Z. Zhang, *et al.*, Effective and structure-controlled adsorption of tetracycline hydrochloride from aqueous solution by using Fe-based metal-organic frameworks, *Appl. Surf. Sci.*, 2021, **542**, 148662.
- 54 S. J. Olusegun, N. D. Mohallem and V. S. Ciminelli, Reducing the negative impact of ceftriaxone and doxycycline in aqueous solutions using ferrihydrite/plant-based composites: mechanism pathway, *Environ. Sci. Pollut. Res.*, 2022, **29**(44), 66547–66561.
- 55 M. Pimentel, *Oxidation of Phenol and Cresol by Electrochemical Advanced Oxidation Method in Homogeneous Medium: Application to Treatment of a Real Effluent of Aeronautical Industry*, Université Paris-Est, 2008.
- 56 D. A. Ghoraba, M. M. Mohamed and O. K. Zaki, Screening of diseases associated with abnormal metabolites for evaluation of HPLC in organic aciduria profiling, *Egypt. J. Med. Hum. Genet.*, 2014, **15**(1), 69–78.

